

Contents

1 Theory	3
1.1 Sesquioxides	3
1.1.1 Chromium Oxide	4
1.1.2 Gallium Oxide	7
1.2 X-ray Diffraction Principles	8
1.2.1 Scattering at Lattices	8
1.2.2 X-rays	9
1.3 Heteroepitaxy	10
1.3.1 Pseudomorphic Growth	10
1.3.2 Relaxed Growth	11
Dislocations	11
Slip Systems for Sesquioxide Heterostructures	12
2 Experimental Methods	15
2.1 Pulsed Laser Deposition	15
2.1.1 Setup	15
2.1.2 Plasma Dynamics	17
2.1.3 Segmented Target Approach	17
2.2 X-Ray Diffraction Measurement	18
2.2.1 2θ - ω -scans	18
2.2.2 ω -scans	19
2.2.3 ϕ -scans	20
2.2.4 Reciprocal Space Maps	20
2.2.5 Technical Details	22
2.3 Further Methods	23
2.3.1 Thermal Evaporation	23
2.3.2 Resistivity Measurement	24
2.3.3 Thickness Determination	25
2.3.4 Spectral Transmission	25
3 Experiment, Results and Discussion	27
3.1 Preliminary Investigations	28
3.1.1 Experiment	28
3.1.2 Oxygen Partial Pressure Variation on <i>m</i> -plane Sapphire	28
3.1.3 Growth Temperature Variation on <i>m</i> -plane Sapphire	33
3.1.4 Influence of Growth Rate on Crystal Structure	33
3.1.5 Deposition on <i>c</i> -, <i>r</i> -, <i>m</i> - and <i>a</i> -plane Sapphire	35
3.1.6 Conclusion	37
3.2 Discrete Combinatorial Synthesis for Taylored Doping	39
3.2.1 Experiment	39

3.2.2	DCS with Different Targets	39
3.2.3	Conclusion	45
3.3	Strain Analysis	48
3.3.1	Experiment	49
3.3.2	Growth Rates	53
3.3.3	Strain and Tilt for Different Orientations	53
3.3.4	Conclusion	67
3.4	Cr ₂ O ₃ Buffer Layers for α -Ga ₂ O ₃	68
3.4.1	Experiment	68
3.4.2	Results	69
3.4.3	Conclusion	74
Appendices		76
A Calculations		77
A.1	<i>m</i> -plane lattice constants	77
A.2	<i>a</i> -plane lattice constants	77
B Figures		79
Bibliography		85

Chapter 3

Experiment, Results and Discussion

Contents

3.1 Preliminary Investigations	28
3.1.1 Experiment	28
3.1.2 Oxygen Partial Pressure Variation on <i>m</i> -plane Sapphire	28
3.1.3 Growth Temperature Variation on <i>m</i> -plane Sapphire	33
3.1.4 Influence of Growth Rate on Crystal Structure	33
3.1.5 Deposition on <i>c</i> -, <i>r</i> -, <i>m</i> - and <i>a</i> -plane Sapphire	35
3.1.6 Conclusion	37
3.2 Discrete Combinatorial Synthesis for Taylored Doping	39
3.2.1 Experiment	39
3.2.2 DCS with Different Targets	39
3.2.3 Conclusion	45
3.3 Strain Analysis	48
3.3.1 Experiment	49
3.3.2 Growth Rates	53
3.3.3 Strain and Tilt for Different Orientations	53
3.3.4 Conclusion	67
3.4 Cr₂O₃ Buffer Layers for α-Ga₂O₃	68
3.4.1 Experiment	68
3.4.2 Results	69
3.4.3 Conclusion	74

3.3 Strain Analysis

The structural properties of the thin film, namely its mosaicity and lattice distortion depend crucially on the growth process: It was observed that the absorption of energy at the laser entrance window alters the growth rate and the crystallinity much more dominantly than the growth temperature or the oxygen partial pressure (cf. chapter 3.1). A similar effect was observed when worn targets were used for fabrication: a non-planar surface caused by tracks that were carved by the laser during previous ablations alter both structural and electrical properties of the resulting thin films substantially (cf. chapter 3.2). Therefore, the following investigations focus on the origin of the observed variations in strain and ω -FWHM. This is further motivated by the observation that a deliberate and controlled variation of laser spot size on the target surface yields a large reduction of ω -FWHM as well as a reduced shift of the peak position in the 2θ - ω -pattern (Fig. 3.20). This was achieved by varying the lens position L such that the laser spot size increases, yielding smaller fluence F and larger ablation area A on the target surface. Namely, doubling the laser spot size from 8 to 16 mm² results in an improvement of crystallinity by a factor of over 5.

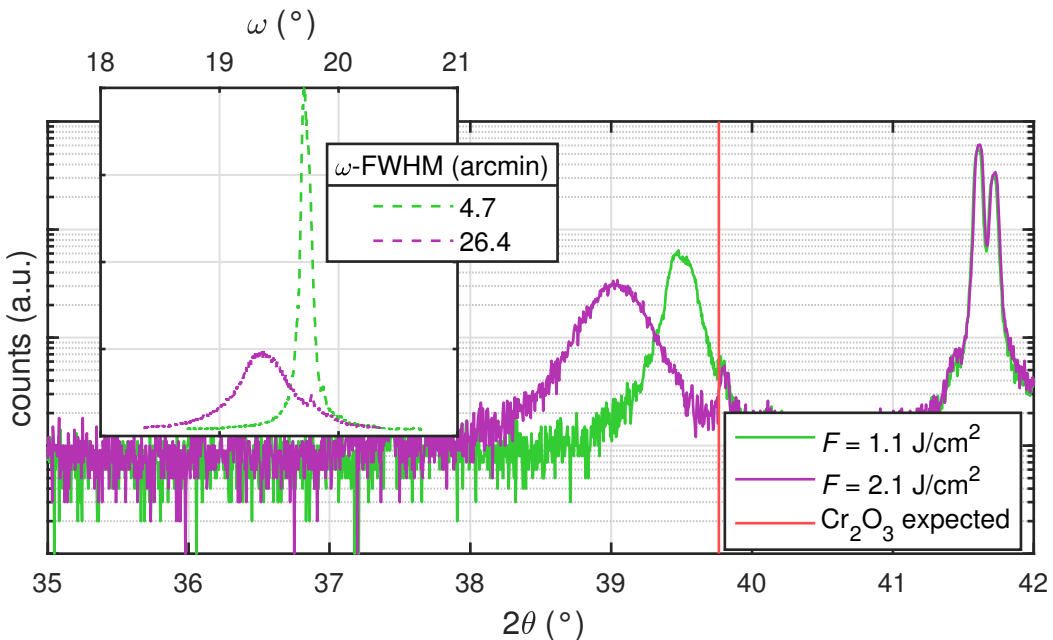


Figure 3.20: 2θ - ω -patterns for two c -plane samples fabricated with different laser spot size, therefore different laser fluence on the target. The thickness is 120 nm and 100 nm for the low fluence (green) and high fluence (purple) sample, respectively. The red line at 39.8° corresponds to the calculated peak position of the Cr_2O_3 (00.6) reflection. The low intensity peak at this angle is the Al_2O_3 (00.6) reflection caused by tungsten La_1 radiation. The peak at approx. 41.5° corresponds to the Al_2O_3 (00.6) reflection caused by copper $\text{K}\alpha$ radiation. The peak at approx. 41.5° corresponds to the Al_2O_3 (00.6) reflection caused by copper $\text{K}\alpha$ radiation. The inset displays the diffractograms of the corresponding ω -scans performed on the Cr_2O_3 (00.6) reflection. The ZnO-doped (low) target (cf. chapter 3.2) was used for deposition without a fixed r_{PLD} but with uniform ablation on the whole target surface. The reason for the choice of target is that this experiment was conducted in the course of the studies of the previous chapter, where a DCS approach was applied for thin film doping. A pulse energy of 650 mJ was applied.

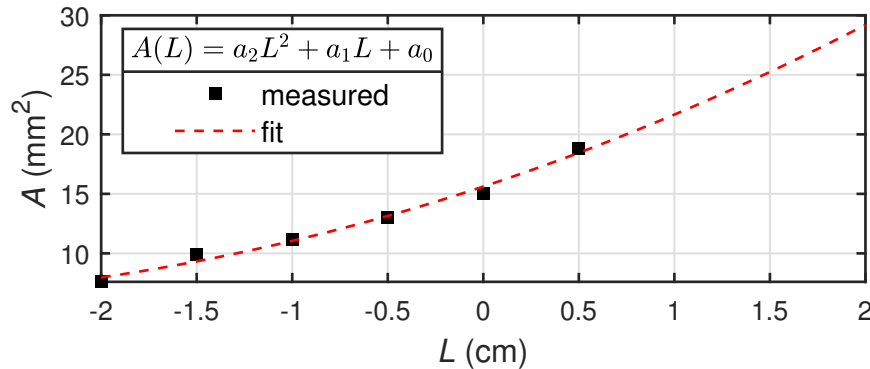


Figure 3.21: Laser spot size A depending on the lens position L : measured data (black) and fit according to $A(L) = a_2 L^2 + a_1 L + a_0$ (red dashed). The fit parameters a_2 , a_1 and a_0 are $0.74 \text{ mm}^2 \text{ cm}^{-2}$, $5.3 \text{ mm}^2 \text{ cm}^{-1}$ and 15.6 mm^2 , respectively.

3.3.1 Experiment

Sample Fabrication

For all following depositions, the laser entrance window was cleaned before each process. A pure Cr_2O_3 target was used for deposition of thin films on $5 \times 5 \text{ mm}^2$ sapphire substrates in the four aforementioned orientations. A first series of samples was produced by only varying the pulse number to achieve a series of thin films with varying thickness but constant laser fluence during deposition. Therefore, the influence of thickness and growth rate can be deconvoluted. The pulse energy was set to 650 mJ and the lens position to -2 cm , resulting in a laser spot size of 8 mm^2 . As described in section 2.1.1, the laser pulse energy inside the PLD chamber is significantly lower than 650 mJ , due to absorption at the mirror, UV lens and laser entrance window. By accounting for this attenuation, the resulting fluence on the PLD target is approx. 2 J cm^{-2} . This corresponds to the standard configuration during all previous processes (pink square in Fig. 3.22). This was repeated for three other lens positions, namely 0 cm , 1 cm and 2 cm , resulting in lower fluences of 1.1 J cm^{-2} , 0.8 J cm^{-2} and 0.6 J cm^{-2} , respectively. In Fig. 3.22, the yellow circles represent the probed laser fluences. This set of samples is referred to as the 1st batch and is listed in Tab. 3.3. The laser spot sizes for different lens positions are depicted in Fig. 3.21.

To investigate the influence of fluence independent of ablation area, a 2nd batch of samples was fabricated with a laser spot size of approx. 10 mm^2 ($L = -1 \text{ cm}$) but varying laser pulse energy: 300 mJ , 450 mJ , 650 mJ and 800 mJ . The achieved fluences are 0.7 J cm^{-2} , 1.0 J cm^{-2} , 1.5 J cm^{-2} and 1.8 J cm^{-2} (red triangles in Fig. 3.22). The pulse number was adjusted to achieve approximately the same thickness for all samples even though the growth rate vastly differs. But note that for the different samples, the thickness is distributed from 100 to 200 nm . Better results could be achieved in future experiments by first calibrating the growth rates for different fluences, and then adjusting the pulse numbers accordingly. The process parameters of those samples are listed in Tab. 3.3.

Measurements

For all samples, 2θ - ω -scans as well as ω -scans were performed. The symmetric reflections probed by the latter were (00.6) , (02.4) , (30.0) and (22.0) for c -, r -, m - and a -plane, respectively. For r - and a -plane samples, the higher order reflection was chosen because the distance between the Cr_2O_3 peak and the Al_2O_3 peak caused by $\text{W-L}\alpha_1$ ra-

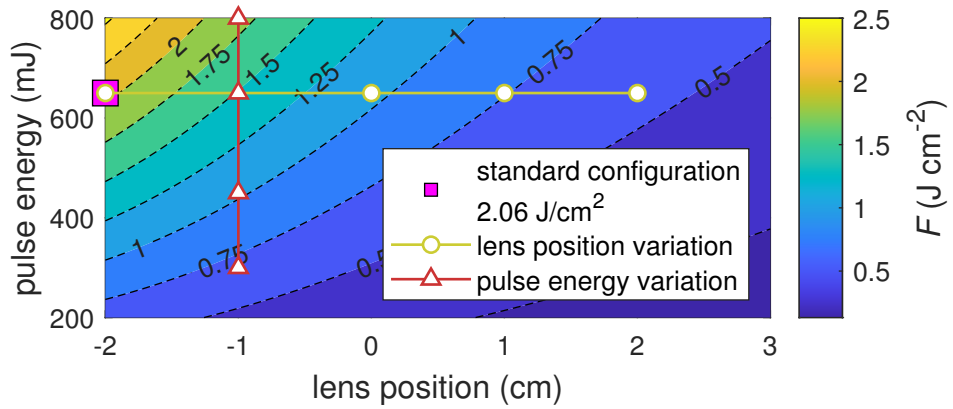


Figure 3.22: Laser energy density depending on the applied pulse energy and lens position. Smaller lens positions yield smaller spot sizes. A value of -2 cm corresponds to the lens being as close as possible to the laser entrance window in the setup used for this work. The default configuration of 650 mJ and -2 cm yields typical fluences of about 2 J cm^{-2} . The triangles and circles represent the variation of laser fluence in this work, achieved by varying the pulse energy and lens position, respectively.

Table 3.3: Processes of the first and second batch. For the first batch, a constant laser pulse energy of 650 mJ was applied. The second batch was obtained by fixing the laser spot size to 10 mm². For every process, Cr₂O₃ was deposited on four sapphire substrates with different orientations of *c*-, *r*-, *m*- and *a*-plane.

L (cm)	E_L (mJ)	A (mm 2)	F (J cm $^{-2}$)	pulses (1k)	t (nm)
Batch 1	-2	8	2.1	5	25
				10	45
				20	80
				40	170
				70	210
	0	16	1.1	8	40
				20	90
				35	40
	1	22	0.8	20	50
				40	65
Batch 2	2	29	0.6	17	30
	-1	300	10	40	90
				70	150
	450		1.0	40	150
				50	150
	650		1.5	40	200
				35	170

diation increases with higher angles. Because both peaks are located at similar angles, this approach reduces the contribution of the substrate to the thin film Rocking curves. To obtain more information about the relation between in-plane and out-of-plane lattice constants, Reciprocal Space Maps (RSMs) were performed on selected samples. For every orientation, lattice planes have been chosen that have both a rather small tilt and high intensity:

c-plane For *c*-plane samples, the thickness series grown at $L = -2\text{ cm}$ and therefore a laser spot size of 8 mm^2 ($F = 2.1\text{ J cm}^{-2}$) of the 1st batch was investigated. The asymmetric reflection that was used for probing the relaxation process is (02.10) , which has an inclination angle of approx. 32° with respect to the sample surface.

r-plane All *r*-plane samples fabricated in the 2nd batch with different laser pulse energies were investigated with RSMs. For each sample, the *x*-axis of the sample – containing the projection of the *c*-axis – is found by performing a ϕ -scan on the (03.0) reflection: This set of lattice planes has an inclination with respect to the surface, so the position of the peak in the diffraction pattern of the ϕ -scan reveals the *x*-axis. In this azimuth, an RSM is recorded around the asymmetric (03.0) reflection and the symmetric (02.4) reflection. By rotating $\Delta\phi = 90^\circ$, the *y*-axis lays in the scattering plane and another RSM is performed around the symmetric (02.4) reflection. The twofold measurement of the symmetric reflection is necessary to calculate a possible lattice plane tilt for both *x*- and *y*-direction. After performing the various corrections described in 2.2.4, the tilt angles can be calculated for both azimuths by

$$\theta = \arccos \left(\frac{q_\perp}{|\mathbf{q}|} \right) \cdot \operatorname{sgn}(q_\parallel), \quad (3.4)$$

with q_\perp and q_\parallel being the out-of-plane (o.o.p.) and in-plane (i.p.) components of the scattering vector \mathbf{q} , respectively. The i.p. and o.o.p. strains are determined by comparing the observed (03.0) scattering vector to the scattering vector calculated from Cr_2O_3 bulk lattice constants:

$$\mathbf{q}_{(03.0)} = |\mathbf{q}_{(03.0)}| \cdot \begin{pmatrix} \cos \alpha_{(03.0)|r} \\ \sin \alpha_{(03.0)|r} \end{pmatrix}, \quad (3.5)$$

with $|\mathbf{q}_{(03.0)}|$ calculated from Equ. (2.6) and Equ. (2.7). $\alpha_{(03.0)|r}$ denotes the angle between the (03.0) reflection and the normal of the *r*-planes; it can be calculated from Equ. (2.8):

$$\alpha_{(03.0)|r} = 90^\circ - (\alpha_{(03.0)|c} - \alpha_{(01.2)|c}) = \alpha_{(01.2)|c} = 57.62^\circ. \quad (3.6)$$

m-plane Similar to the *r*-plane samples, all *m*-plane samples from the 2nd batch were investigated. The samples were aligned to the *x*-axis by performing a ϕ -scan on the asymmetric (30.6) reflection, and an RSM was recorded afterwards. By rotating $\Delta\phi = 180^\circ$ while maintaining 2θ and ω , the scattering condition for $(30.\bar{6})$ is probed and an RSM was recorded. The symmetric reflection (30.0) was also measured in this azimuth. The tilt angle and shear angle can be calculated according to Equ. (3.4) and Equ. (2.13), respectively. As described in further detail in appendix A.1, the lattice

constants can be calculated from the components of the scattering vectors:

$$a_{\perp} = \frac{\sqrt{12}}{q_{\perp}^{(30.\pm 6)}} , \quad (3.7)$$

$$a_{\perp} = \frac{\sqrt{12}}{q_{\perp}^{(03.0)}} , \quad (3.8)$$

$$c = \frac{6}{q_{\parallel}^{(30.\pm 6)}} . \quad (3.9)$$

a_{\perp} denotes the a lattice constant in direction of the normal to the sample surface. By rotating $\Delta\phi = 90^\circ$, the y -axis can be probed via asymmetric reflections $(\bar{4}2.0)$ and (22.0) , which differ in the azimuth by $\Delta\phi = 180^\circ$. A second symmetric reflection (30.0) is recorded in this azimuth. Similar to the x -axis, the tilt and shear angles, as well as the lattice constants can be calculated:

$$(4\bar{2}.0) : \quad a_{\perp} = \frac{\sqrt{12}}{q_{\perp}^{(4\bar{2}.0)}} , \quad a_{\parallel} = \frac{2}{q_{\parallel}^{(4\bar{2}.0)}} , \quad (3.10)$$

$$(22.0) : \quad a_{\perp} = \frac{\sqrt{12}}{q_{\perp}^{(22.0)}} , \quad a_{\parallel} = \frac{2}{q_{\parallel}^{(22.0)}} , \quad (3.11)$$

$$(30.0) : \quad a_{\perp} = \frac{\sqrt{12}}{q_{\perp}^{(03.0)}} . \quad (3.12)$$

a_{\parallel} denotes the a lattice constant parallel to the y -axis. For detailed calculations of the former equations, see A.1. Note that all 6 measured reflections yield a value for a_{\perp} , and 2 measured reflections each yield 2 values for c and a_{\parallel} , respectively. Therefore, for each lattice constant, the mean value is evaluated and the error is estimated by the standard deviation (cf. Fig. 3.34a).

a -plane All a -plane samples from the 2nd batch were investigated and the method is similar to the one applied to the m -plane samples. The azimuth of the x -axis is found by performing a ϕ -scan on the (22.6) reflection, which also served for an RSM. Rotating by $\Delta\phi = 180^\circ$ yields the $(22.\bar{6})$ reflection and (22.0) is also measured. Similar to above, the sample is rotated by 90° to align to the y -axis and two more asymmetric reflections are recorded: (30.0) and (03.0) . A second RSM of (22.0) is also performed. This yields the following lattice constants for the x -axis:

$$a_{\perp} = \frac{4}{q_{\perp}^{(22.\pm 6)}} , \quad (3.13)$$

$$a_{\perp} = \frac{4}{q_{\perp}^{(22.0)}} , \quad (3.14)$$

$$c = \frac{6}{q_{\parallel}^{(22.\pm 6)}} , \quad (3.15)$$

and for the y -axis:

$$(30.0) : \quad a_{\perp} = \frac{3}{q_{\perp}^{(30.0)}} \quad , \quad a_{\parallel} = \frac{3}{\sqrt{3}q_{\parallel}^{(30.0)}}, \quad (3.16)$$

$$(03.0) : \quad a_{\perp} = \frac{3}{q_{\perp}^{(03.0)}} \quad , \quad a_{\parallel} = \frac{3}{\sqrt{3}q_{\parallel}^{(03.0)}}, \quad (3.17)$$

$$(22.0) : \quad a_{\perp} = \frac{4}{q_{\perp}^{(22.0)}}. \quad (3.18)$$

For detailed calculations, see A.2. Again, for the lattice constants obtained from several reflections, the mean and standard deviation are calculated (cf. Fig. 3.34b).

3.3.2 Growth Rates

In Fig. 3.23, a detailed view into the growth rates of the samples of the 1st batch is given. First of all, for a fixed fluence (false color), increasing the pulse number decreases the growth rate. This is expected, because the coating of the laser entrance window increases during the process. By fixing a pulse number to 20 000 pulses, an increase in growth rate is observed for a regime of decreasing fluence from 2 to 1 J cm⁻² (Fig. 3.23 bottom). This can be explained by the fact that the reduction of fluence is due to increasing laser spot size. When the fluence is still above the ablation threshold for the target material, an increasing ablation area results in an increasing growth rate. But at some point, the fluence is too low to ablate the material and then the growth rate decreases, even though the ablation area increases. This can be observed at around 1.2 J cm⁻² in Fig. 3.23, which is therefore an estimate for the ablation threshold. For the growth rates of the samples of the 2nd batch (Fig. 3.24), a similar conclusion can be drawn. Reducing the fluence via decreasing laser pulse energy below approx. 1.5 J cm⁻² results in a decrease of growthrate from 5 to 2 pm pulse⁻¹. The ablation threshold can be localized between 1 J cm⁻² and 1.5 J cm⁻², which is in accordance to the value obtained for the 1st batch.

3.3.3 Strain and Tilt for Different Orientations

c-plane: Laser Spot Size Variation

The o.o.p. strain calculated via Equ. (3.1) for all samples of the 1st batch is displayed in Fig. 3.25. Consider the *c*-plane oriented samples of the 1st batch that had a fixed lens position yielding a fluence of approx. 2 J cm⁻², but varying thickness (brown squares in Fig. 3.25). A clear dependence of the o.o.p. strain can be observed: thinner samples yield higher strain. The layers become relaxed for thicknesses above approx. 170 nm. For low thicknesses, the strain approaches the predicted value for pseudomorphic growth of Cr₂O₃ on Al₂O₃, which is 3.90 % (cf. Tab. 1.4). The recorded RSMs of the (02.10) reflection can confirm that this observation of o.o.p. strain is due to pseudomorphic growth. In Fig. 3.26, one can observe a shift of $q_{\parallel}^{(02.10)}$ to higher values for lower thicknesses. This corresponds to a decrease of the i.p. lattice constant, which is the expected behavior for pseudomorphic growth, because the i.p. *a* lattice constant of *c*-oriented Al₂O₃ is 0.2 Å smaller than for Cr₂O₃ (cf. Tab. 1.1). The tensile o.o.p. strain observed via 2θ-ω-scans can also be confirmed by the fact that the o.o.p. component $q_{\perp}^{(02.10)}$ is decreasing for thinner samples. The reduction of signal intensity is attributed to the thickness, but could also be a result of decreasing crystal quality (cf. Fig. 3.27). **makushko2022** reported a similar behavior for *c*-plane Cr₂O₃ thin films deposited

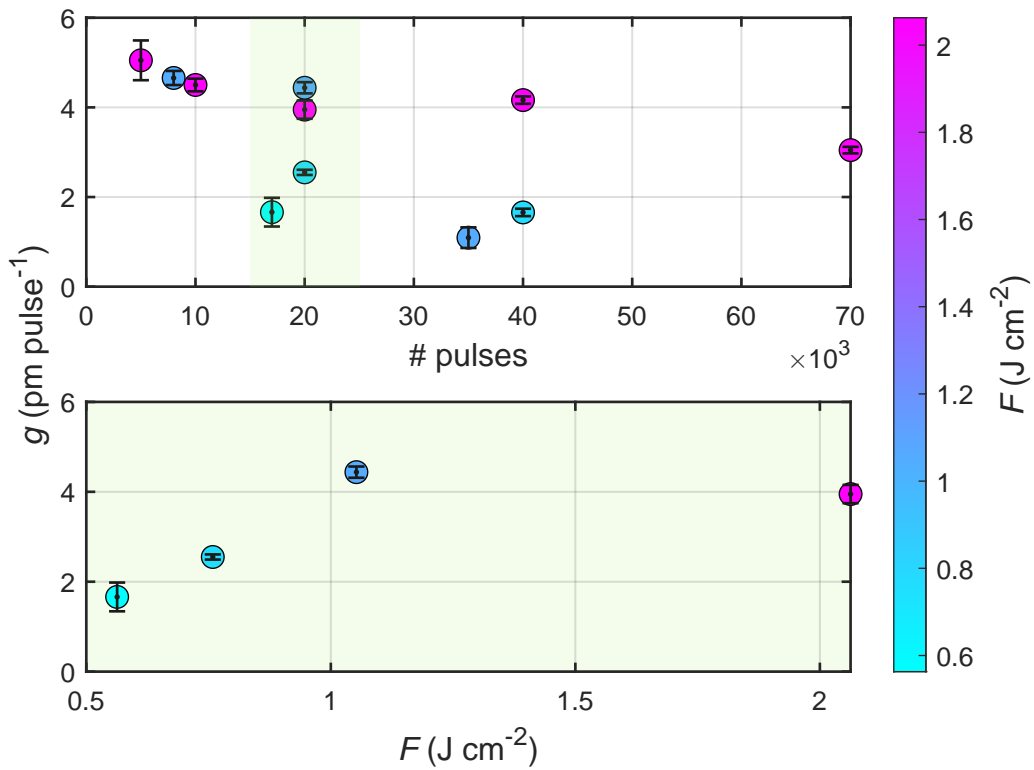


Figure 3.23: Growth rates of the samples from the 1st batch, i.e. samples with different laser spot size and therefore different laser fluence (false color), as well as different pulse number each (cf. Tab. 3.3). The growth rate is visualized as depending on the pulse number (top) and depending on the laser fluence on the target for a fixed pulse number of 20 000 (bottom). The data points are the mean of the four samples with c -, r -, m - and a -orientation, that were obtained from every process. The errorbar displays the standard deviation. s

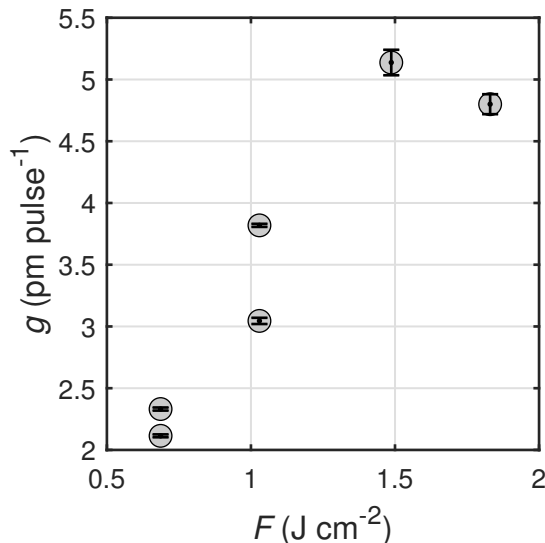


Figure 3.24: Growth rates of samples from the 2nd batch, i.e. samples with different laser pulse energy, but same laser spot size on the target, depending on laser fluence on the target surface. The data points are the mean of thicknesses of the four orientations, similar to Fig. 3.23.

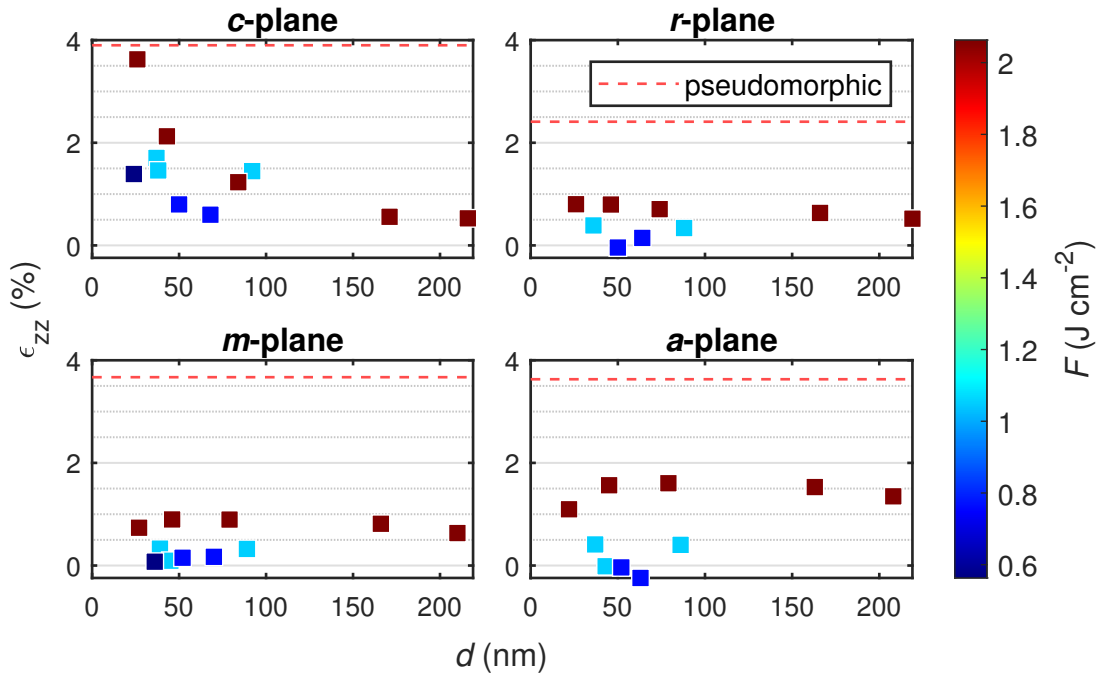


Figure 3.25: Out-of-plane strain calculated from $2\theta\text{-}\omega$ -patterns for all samples from the 1st batch, depending on thickness and laser fluence (false color).

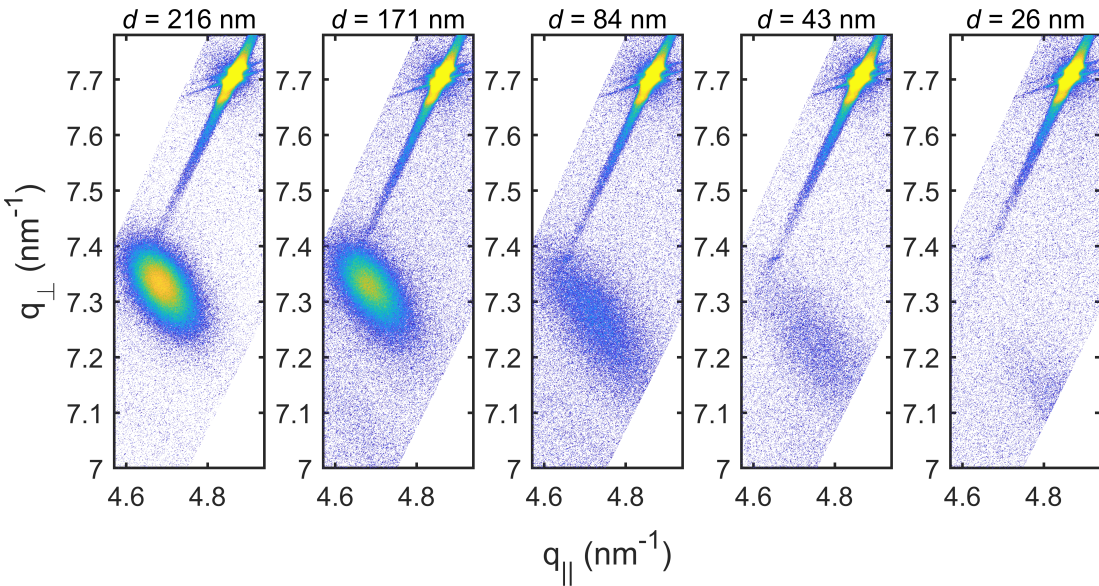


Figure 3.26: RSMs of the (02.10) reflection for *c*-plane oriented samples with varying thickness. The laser spot size was 8 mm^2 , resulting in a fluence of approx. 2 J cm^{-2} . The reflection in the upper right corner corresponds to the (02.10) reflection of the sapphire substrate.

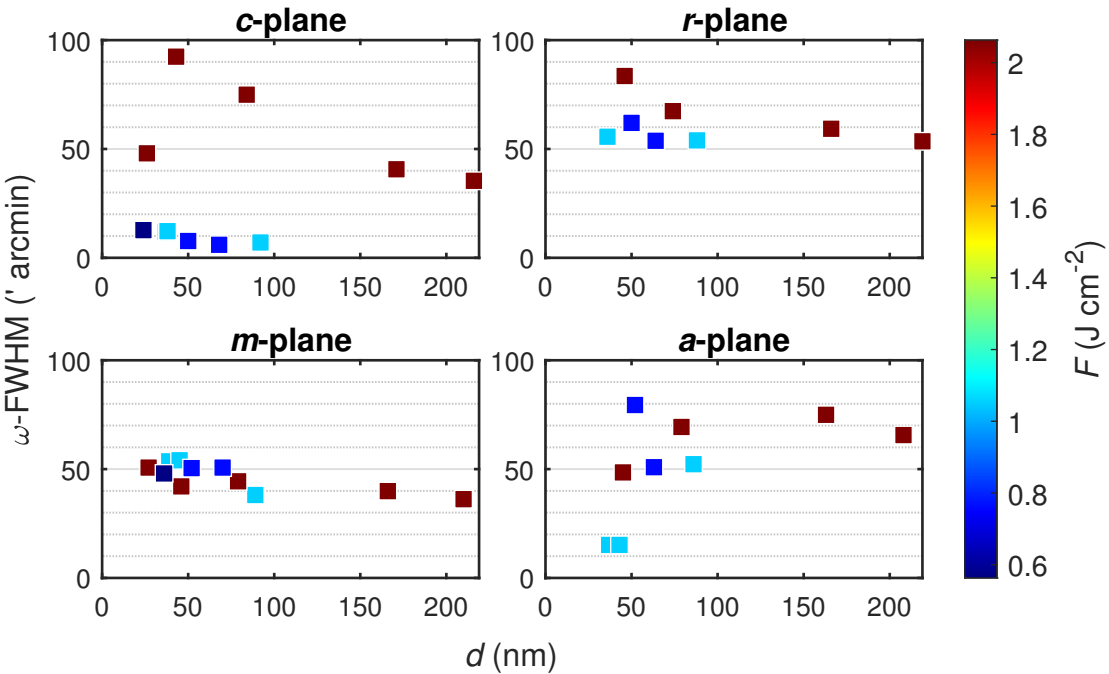


Figure 3.27: ω -FWHM for all samples from the 1st batch, depending on thickness and laser fluence (false color). The corresponding diffractograms are depicted in Fig. B.4.

via magnetron sputtering. They also varied the thin film thickness from 30 to 250 nm. In Transmission Electron Microscopy (TEM) measurements, they could observe that dislocations started forming approx. 5 nm away from the Cr_2O_3 – Al_2O_3 interface, indicating a highly strained pseudomorphic layer. This could also be observed as a very sharp peak in reciprocal space, identified by an alignment of q_{\parallel} with a corresponding asymmetric substrate reciprocal space vector. Note that this peak cannot be observed for the here presented samples. A reason for this could be that **makushko2022** observed this for thin films with thickness of 30 nm only. Almost every thin film presented here exceeds this critical thickness. Another reason could be that the probed plane was the $(10.\bar{1}0)$ reflection, which

When looking into the remaining samples that were fabricated with larger laser spot sizes but similar thickness of 50 nm (bluish squares in Fig. 3.25), it becomes clear that the o.o.p. strain is also slightly reduced for lower fluences. But note that this effect is less dominant when compared to the influence of thickness.

In Fig. 3.27, the ω -FWHM is depicted in dependence on the film thickness and laser fluence for the 1st batch. As before, consider the samples with smallest laser spot size (largest fluence) first: increasing the thickness is clearly correlated to a decreasing ω -FWHM. Therefore, thicker samples yield *both* less strained and more crystalline films. This is an unexpected result, because as shown in section 1.3.2, relaxation is mediated by dislocations which should worsen the crystal quality. Note that there is an outlier to this behavior for the sample with a thickness of approx. 30 nm. When considering the ω -pattern of this sample (Fig. B.1a), it becomes clear that the non-VOIGT shape makes the determination of Full Width at Half Maximum (FWHM) difficult. Therefore, not too much attention should be paid to this data point. When considering the samples fabricated with lower fluences (bluish squares in Fig. 3.27), a much more dominant influence of laser spot size on the crystallinity can be observed. This can be summarized by stating that the thickness of the samples is the dominant influence on the o.o.p. strain, because the thickest samples yielded less strain than the thinner samples with lowest fluence (Fig. 3.25). However, for the ω -FWHM, the

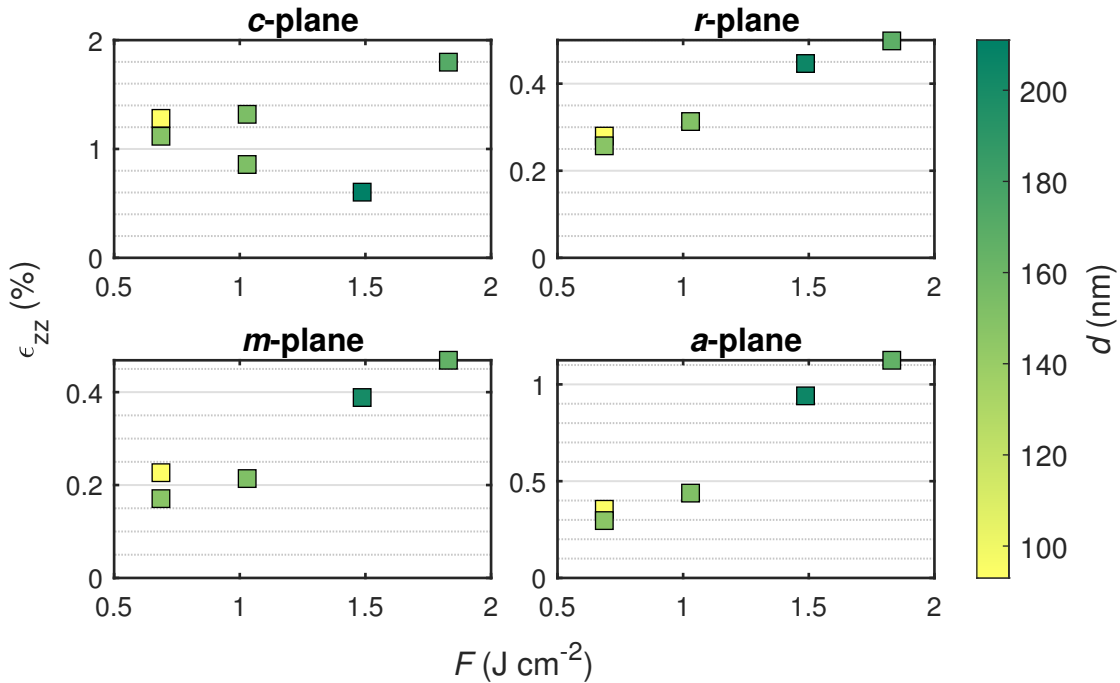


Figure 3.28: Out-of-plane strain calculated from $2\theta\text{-}\omega$ -patterns for all samples from the 2nd batch, depending on laser fluence and thickness (false color).

reverse is observed, namely that even the thickest samples (which exhibit better quality than thinner samples of the same lens position) have a much higher ω -FWHM when compared to thinner samples fabricated with less fluence. This can be seen in Fig. B.2, where the ω -FWHM is visualized depending on the o.o.p. strain of the corresponding sample: A linear behavior (correlation) is observed for each set fluence; but there are two different regimes in total, with the high-fluence regime generally showing higher ω -FWHM.

c-plane: Pulse Energy Variation

The o.o.p. strain for the *c*-plane oriented samples fabricated with various laser pulse energies, but constant laser spot size, are depicted in Fig. 3.28. Note that there is still a distribution of thickness from 100 to 200 nm, even though it was tried to counteract this by adjusting the pulse numbers. Therefore, the thickness is also displayed via false color to account for the convolution of thickness with laser fluence. The strain is overall smaller (< 2 %) than for the 1st batch, because the 2nd batch contained samples with thickness $t > 100$ nm which yields smaller strains as seen before. No systematic dependence on the laser fluence is observed, which may be explained by the still remaining thickness distribution which overlaps the fluence variation. This effect could be strong enough to overshadow the impact of laser pulse energy, as it was shown in the previous experiments that the thickness is the dominant factor for the o.o.p. strain. For example, note the sample fabricated with $F = 1.5 \text{ J cm}^{-2}$ (dark green square in Fig. 3.28), which exhibits the lowest strain, even though having higher fluence value than other samples. This can be explained by the fact that with $t = 200$ nm, it is the thickest sample of the batch and therefore the lowest strain is expected (cf. Fig. 3.25).

In Fig. 3.29, the ω -FWHM is depicted depending on the laser fluence and film thickness for the 2nd batch. The previously observed relation is confirmed: increasing fluences result in higher ω -FWHMs. Namely, reducing the fluence by a factor of 2

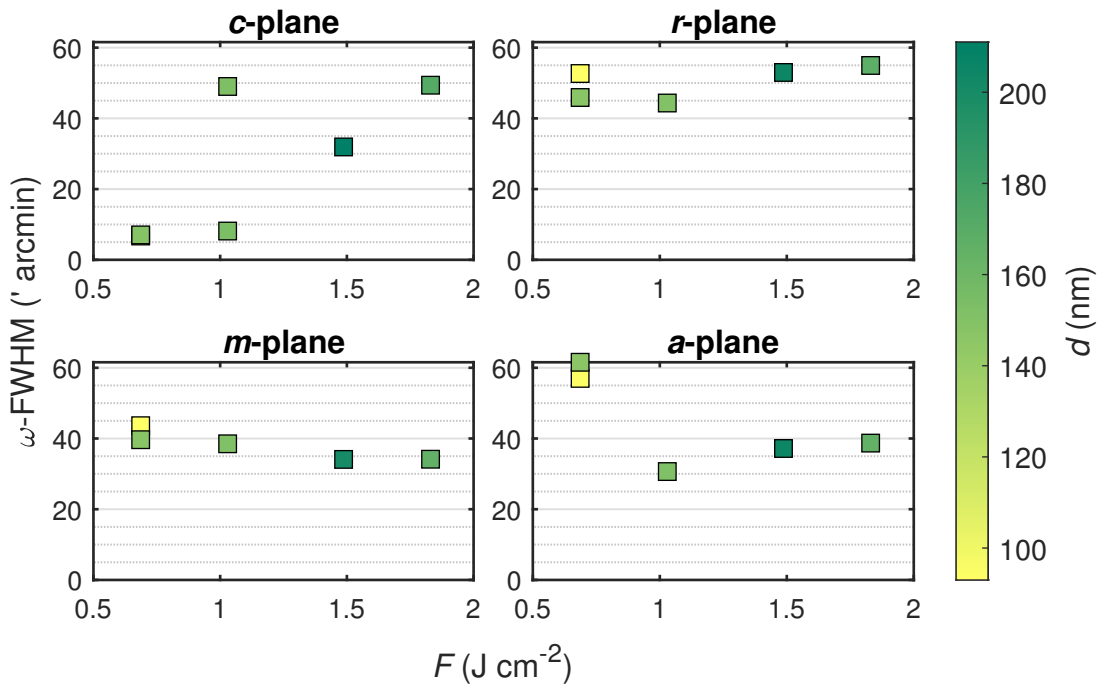


Figure 3.29: ω -FWHM for all samples from the 2nd batch, depending on laser fluence and thickness (false color). The corresponding diffractograms are depicted in Fig. B.5.

results in a crystal quality improvement by one order of magnitude. Note that for a fluence of approx. 1 J cm^{-2} , two samples A and B with same thickness of 150 nm exhibit very different ω -FWHM of $\Delta\omega_A = 8'$ and $\Delta\omega_B = 49'$. The ω -patterns are depicted in Fig. B.1b. Note that both diffractograms have VOIGT shape, so the discrepancy may not be attributed to the determination of the FWHM. On the contrary, note that for the whole process B, which represents a set of samples with *c*-, *r*-, *m*- and *a*-orientation, a determination of FWHM was possible only for the *c*-plane samples⁽⁵⁾. In Fig. B.3, the ω -patterns of samples of all orientations from this process are depicted. The non-VOIGT shape for the orientations other than *c*-plane as well as the unexpectedly high ω -FWHM for *c*-plane sample indicate that the process yielded samples with poor crystal quality. The origin of this observation is not entirely clear, but since both A and B were conducted with the same process parameters with similar growthrate of $g_A = 3 \text{ pm pulse}^{-1}$ and $g_B = 3.75 \text{ pm pulse}^{-1}$, an effect must have influenced the thin film deposition substantially.

***r*-plane: Laser Spot Size Variation**

In Fig. 3.25, the o.o.p. strain for the *r*-plane samples fabricated with varying laser spot size is shown. The overall strain is less than 1% and lower when compared to the *c*-plane samples, exhibiting values up to 4% for thin samples. In particular, the predicted value for o.o.p. strain during pseudomorphic growth of Cr_2O_3 on Al_2O_3 of 2.41% is not reached (cf. Tab. 1.4). As can be seen in a detailed view (Fig. B.6), the strain depends on the thickness: it decreases from 0.8% to 0.5% for an increment of thickness from 50 nm to 200 nm. This is in accordance to the behavior observed for the *c*-plane samples, albeit less pronounced. Furthermore, for a fixed thickness, decreasing the fluence also results in less strained thin films, which is similar to the behavior of the *c*-plane samples. The ω -FWHM obtained from the (02.4) reflection is

⁽⁵⁾ This is why in Fig. 3.29, only the upper left *c*-plane tile has two data points at $F \approx 1 \text{ J cm}^{-2}$.

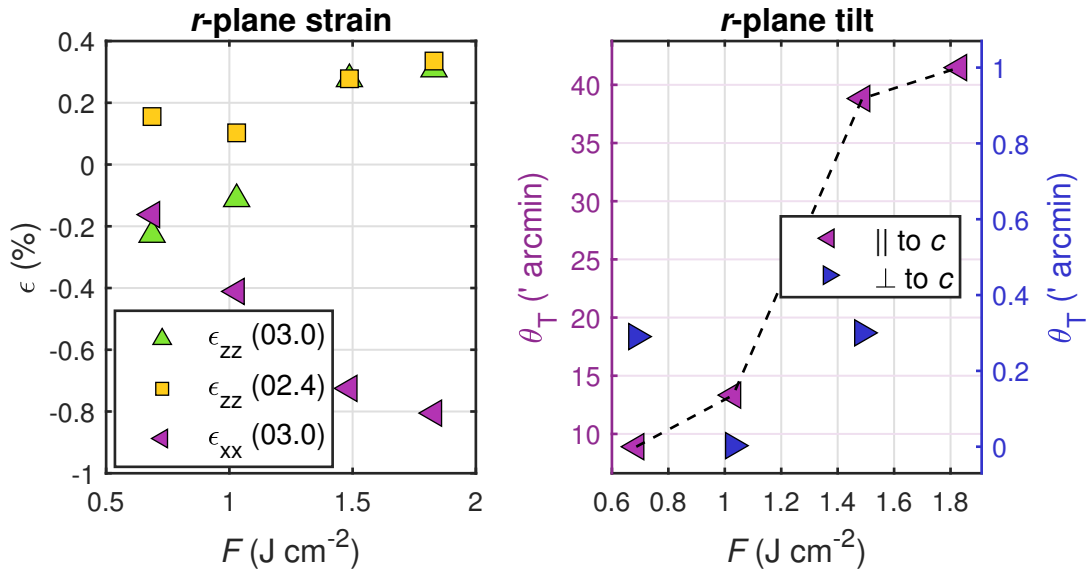


Figure 3.30: In-plane and out-of-plane strain for the r -plane samples from the 2nd batch, calculated from the peak positions of the RSMs described in 3.3.1 (left). Tilt along the x -axis (purple ordinate) and y -axis (blue ordinate), determined from symmetric reflections (right). Note the different scaling of the ordinates, indicating less tilt along the y -axis.

depicted in Fig. 3.27. Similar to the c -plane samples – but less pronounced –, increasing the thickness results in less mosaicity, which is also achieved by reducing the fluence. Note that the overall ω -FWHM is between $50'$ and $90'$ which is significantly higher than for the c -plane samples, where a lower fluence yielded samples with $\Delta\omega < 10'$ (cf. Fig. 3.27). Therefore, increasing the thickness and reducing the fluence by varying laser spot position may increase the crystal quality, but not to an amount comparable to c -plane oriented thin films.

r -plane: Pulse Energy Variation

In Fig. 3.28, the o.o.p. strain is depicted for varying laser pulse energies (2nd batch). Independent of thickness, the fluence determines the strain of the thin films. The overall strain is below 0.4 %, and thereby comparable to the samples obtained from processes in the 1st batch with larger laser spot sizes. A detailed view on the strain for those samples is given in Fig. 3.30 which is based on the evaluation of RSMs that were performed as described in 3.3.1. The o.o.p. strain was calculated from both asymmetric (green triangle) and symmetric (yellow squares) reflections. The latter is equivalent to the calculation from the peak position in 2θ - ω diffraction patterns. It can be observed that the increasing tensile o.o.p. strain comes along with an increasing i.p. compressive strain, ranging from -0.2% to -0.8% . Therefore, the o.o.p. strain may be attributed to a partial pseudomorphic growth mode, because the Al_2O_3 lattice constants are smaller than the ones for Cr_2O_3 . The compressive strain is then due to an aligning of in-plane lattice constants.

Note that the values for o.o.p. strain obtained from 2θ - ω -scans (cf. Fig. 3.28) are only qualitatively confirmed: the strain measured from the symmetric RSM is approx. 0.2 percentage points below the value obtained from 2θ - ω -scans. A comparison of both methods is given in Fig. 3.31, where both a 2θ - ω pattern and a symmetric RSM of the are depicted for one sample ($F = 1.1 \text{ J cm}^{-2}$), as well as the calculated strain for all samples with different laser pulse energy. The origin of this discrepancy may lie

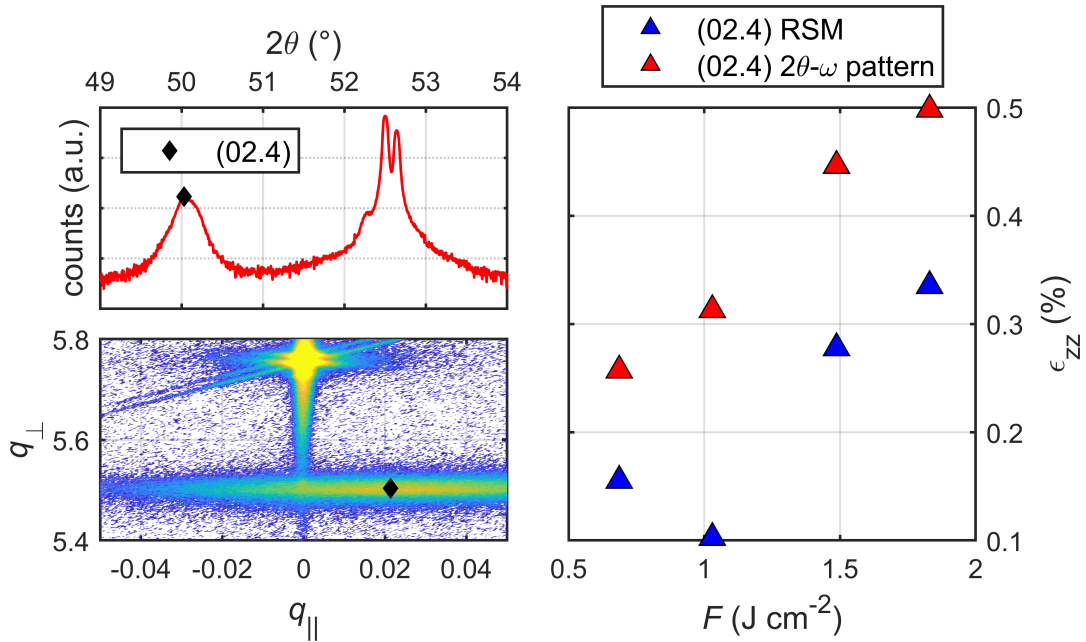


Figure 3.31: Out-of-plane strain for the r -plane samples fabricated with varying laser pulse energy (right). For the sample with $F = 1.1 \text{ J cm}^{-2}$, the $2\theta-\omega$ pattern (top left) and RSM (bottom left) are depicted. The black diamond (\blacklozenge) marks the position of the (02.4) reflection in the 1D $2\theta-\omega$ pattern and 2D RSM.

in on of the corrections that was applied the RSMs, but not to the $2\theta-\omega$ patterns. However, the correction of the substrate peak position in 2D reciprocal space (rotation and stretching, cf. section 2.2.4) corresponds to a shift of the whole 1D $2\theta-\omega$ pattern to match the substrate peak. The latter was done for the evaluation of $2\theta-\omega$ -scans on which Fig. 3.28 is based. But the correction of thin film tilt which is done for RSMs was not done for the $2\theta-\omega$ -scans. This can be seen in Fig. 3.31, where the $2\theta-\omega$ pattern corresponds to a line with $q_{\parallel} = \text{const.} = 0$ in the reciprocal space. The peak on this line has the same q_{\perp} coordinate as the RSM peak not corrected to thin film tilt (both visualized as black diamonds, \blacklozenge). But if the (03.0) peak is rotated by the value of thin film tilt (counterclockwise), the q_{\perp} component slightly increases. Therefore it follows that

$$q_{\perp}^{\text{RSM,corrected}} > q_{\perp}^{\text{RSM,uncorrected}} = q_{\perp}^{2\theta-\omega},$$

which results in a smaller o.o.p. lattice constant obtained from RSMs. Therefore, the o.o.p. strain is smaller, when determined from symmetric RSMs. Note that a ω -optimization prior to a $2\theta-\omega$ -scan is done for correcting a tilt of the *substrate*, which is different from the correction of thin film tilt.

But even though this is a significant difference in evaluation between $2\theta-\omega$ -patterns and RSMs, the discrepancy between both methods does not change significantly when the thin film tilt decreases from $40'$ to $10'$. So further analysis has to be done for the applied evaluation methods. In general it has to be noted that the precision of the o.o.p. strain obtained from RSMs depends on (i) the peak position of the reflection, (ii) the peak position of the corresponding substrate peak (for substrate correction) and (iii) the peak position of the asymmetric peaks (for shear correction, not done for r -plane). These values are subject to a certain amount of uncertainty, which results in an ill-defined error.

Another observation is that the o.o.p. strain obtained from symmetric (yellow squares) and asymmetric reflections (green triangles) aligns for the two samples fab-

ricated with higher fluences only (cf. Fig. 3.30). The discrepancy observed for the lower fluences is unexpected. In Fig. 3.32, all symmetric and asymmetric RSMs are displayed. For the samples fabricated with 650 mJ and 800 mJ, accounting for the thin film tilt will result in a counterclockwise rotation of the reciprocal space. Therefore, the observed (03.0) reflection (■) has a smaller q_{\perp} component compared to the predicted (◆) peak position (after rotation). This results in tensile (positive) strain – which is in accordance with the values obtained from both symmetric RSM reflections and $2\theta\text{-}\omega$ patterns. For the samples with 300 mJ and 450 mJ, however, the thin film tilt is sufficiently small to result in compressive (negative) strain, i.e. the rotation of reciprocal space does not result in a smaller out-of-plane component q_{\perp} of the thin film (■) compared to the bulk value (◆).

and is probably due to an error in evaluation of the RSMs. This is supported by the fact that for those two data points, the strain obtained from asymmetric reflections is almost exactly mirroring the value obtained from the symmetric reflections.

As predicted by Grundmann and Lorenz [1], partially relaxed *r*-plane thin films should exhibit a tilt of the thin film with respect to the substrate. This tilt is indeed observed along the *x*-axis for all values of fluence, ranging from approx. 10' to 40' (purple triangles in Fig. 3.30). A corresponding tilt along the *y*-axis is not observed: there, the tilt angles are two orders of magnitude lower and below 0.4'. This is in agreement with elasticity theory which predicts a tilt only along the *x*-axis, because the prismatic slip systems responsible for relaxation along the *y*-axis yield tilt components of the BURGER's vector that cancel out on average (cf. section 1.3.2). But note that the thin film tilt increases for higher fluences, which also results in a higher o.o.p. strain. This observation is unexpected, because the thin film tilt is a result of *relaxation*, whereas strain is a result of partial *pseudomorphic* growth. So according to strain, higher fluences result in less relaxed layers – according to tilt, higher fluences result in more relaxed layers. This result indicates that an interplay of both processes is present and that for growth modes that exhibit no partially relaxed behavior, more sophisticated models for the relaxation mechanism must be applied.

The ω -FWHM of the *r*-plane samples of the 2nd batch is approx. 50' and has no significant dependence on both fluence or thickness (Fig. 3.29). This confirms the previously obtained result for the samples fabricated with varying laser spot sizes.

***m*- and *a*-plane: Laser Spot Size Variation**

In Fig. 3.25, the o.o.p. strain for the *m*- and *a*-plane oriented samples of the 1st batch (laser spot size variation) is depicted. The maximum strain which is reached for high fluences is approx. 0.8 % and 1.5 % for *m*- and *a*-plane, respectively. Those values are far below the predicted values for pseudomorphic growth, which are 3.67 % (*m*-plane) and 3.63 % (*a*-plane). This indicates relaxed growth. In Fig. B.6 it can be seen that for higher thicknesses, the strain reduces only very slightly. The *m*-plane outlier at a thickness of 25 nm can be explained by the very low peak intensity of the (30.0) reflection in the $2\theta\text{-}\omega$ pattern, which causes a larger uncertainty for this value. Overall, the fluence is the determining parameter for the strain, allowing strain values of down to 0 % for *a*-plane samples.

In Fig. 3.27, the ω -FWHM for both *m*- and *a*-plane samples is depicted. For *m*-plane, the ω -FWHM is approx. 50' for all fluences and thicknesses – only a small decrease for higher thicknesses is observed. As a result, in Fig. B.2, two regimes of high and low fluence can be distinguished, where each regime itself comes with a correlation indicating better crystallinity with less strain. However, altogether, a slight

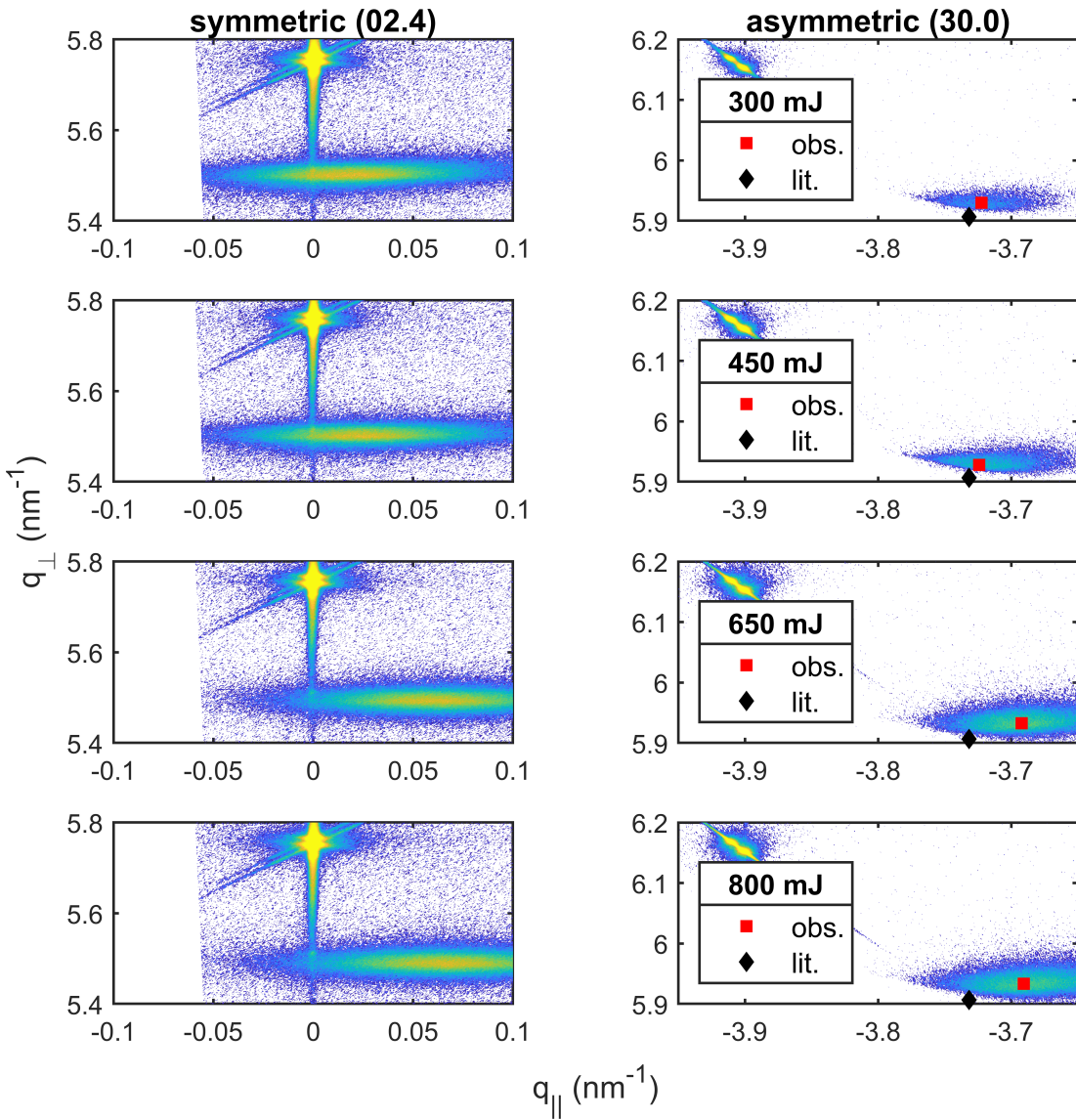


Figure 3.32: Reciprocal space maps of four *r*-plane oriented thin films fabricated with different laser pulse energy. The probed reflections are symmetric (02.4) (left) and asymmetric (30.0) (right). The peak with larger q_{\perp} component corresponds to the substrate. For the RSMs of the asymmetric reflections, the expected peak position (\blacklozenge) as well as the observed peak positions (\blacksquare) are indicated. Note that the RSMs are already corrected such that the substrate peak aligns with the expected position. A thin film tilt is indicated by the nonzero in-plane component of the symmetric (02.4) reflection. For determination of thin film lattice constants, the RSM is rotated by the observed thin film tilt, which is not visualized in these images.

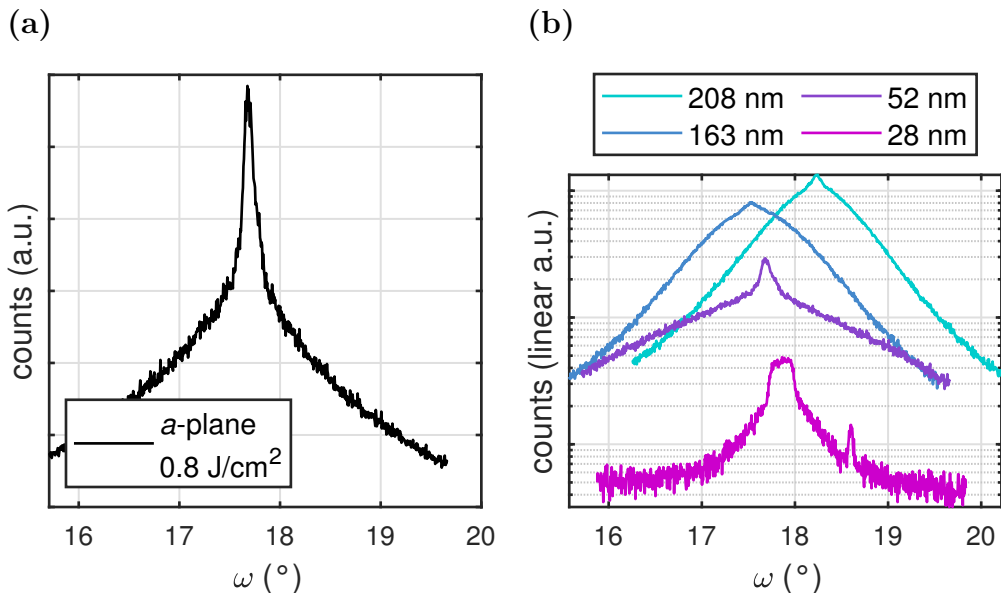


Figure 3.33: ω -pattern of a -plane samples from the 1st batch: (a) a sample with linear representation and (b) samples with varying thickness in logarithmic representation.

negative correlation can be observed, i.e. better crystallinity comes at the cost of higher strain. For a -plane samples, no significant dependence on fluence can be observed. On the contrary, there seems to be an increase in ω -FWHM for increasing thicknesses up to approx. 100 nm. This behavior differs from all other orientations observed and could be attributed to an unusual shape of the ω -patterns. In Fig. 3.33, such a pattern is depicted and has clearly no VOIGT-shape. Rather, the pattern consists of an exponential tail (linear in logarithmic intensity axis) for about 1.5° and a very sharp 2nd peak with a small FWHM on top of it. This shape is observed for almost every a -plane sample, as can be seen by the various diffractograms shown in Fig. B.4. The sharp peak is located at the maximum of the underlying broader peak and can therefore not be attributed to Al_2O_3 or another phase of Cr_2O_3 , because then it would not shift together with the (22.0) peak of the α -phase of Cr_2O_3 . This is also supported by the fact that no anomaly is observed in the 2θ - ω -patterns (not shown). This behavior has previously been observed for ZnO thin films grown on c -plane silicon [2, 3]. There, the broader peak contribution is attributed to a degradation at the interface region [2] and the sharp peak is present for a weakly disordered film, where the misfit to the substrate is damped through the underlying film. As shown by Durand *et al.* [3], the ω -FWHM of the narrow peak is limited by the instrumental resolution – they could resolve a broadening of 5 arcseconds for this peak. This behavior has also been observed for c -plane oriented Cr_2O_3 thin films fabricated by PLD [4]. In Fig. 3.33b, several ω -patterns are depicted for thin films of different thickness. For a layer thickness of 30 nm, a broad peak with an overlaying higher intensity peak is observable, which is not narrow but exhibits a plateau with a width of approx. 0.25° . For increasing film thicknesses, the FWHM of both the broader and narrow peak decrease, confirming the growth of a higher crystalline layer. Henceforth, the crystallinity of a -plane Cr_2O_3 thin films should be assessed by a two-layer model when determining the FWHM of the corresponding ω patterns.

***m*- and *a*-plane: Pulse Energy Variation**

In Fig. 3.28, the o.o.p. strain for the *m*- and *a*-plane oriented samples of the 1st batch is depicted. The strain ranges from 0.15 % (0.3 %) to 0.45 % (1.1 %) for *m*-plane (*a*-plane) samples. A clear dependence on fluence can be observed, whereas the thickness has no influence on the o.o.p. strain at all. The complete in- and out-of-plane strains for *m*-plane samples are depicted in Fig. 3.34a. With increasing o.o.p. strain, the i.p. strain also increases, which indicates a pseudomorphic growth mode. Note that the i.p. strain is, in the range of uncertainty, the same along both *x*- and *y*-direction, even though both axes are not equivalent. As for *r*-plane samples (cf. Fig. 3.30), the o.o.p. strain is systematically smaller by 0.15 percentage points, compared to the values obtained from peak positions in 2θ - ω -patterns (Fig. 3.28). 2θ - ω -scans probe for symmetric reflections only, which is why shear stresses cannot be corrected by this method. However, those angles are rather small (< 3°, cf. Fig. 3.34a), which is why it is unfeasible that this is the origin of the discrepancy. Moreover, as discussed for the *r*-plane samples, a thin film tilt can be observed, but the discrepancy does not change with varying tilt angles, which makes a correlation between both implausible.

As predicted by Grundmann [5] and demonstrated by Kneiß *et al.* [6], a significant tilt of the thin film is observed along the *x*-direction (purple triangles in Fig. 3.34a), which ranges from 20' to 40' and increases with higher fluences. Furthermore, a small shear Ψ_S of up to 2' is observed along this axis. On the contrary, a thin film tilt and a shear tilt below 1' are observed in *y*-direction (not shown). This is also in accordance with the predicted slip systems (cf. 1.3.2), which should result in no net tilt along the *y*-axis. However, as it is the case for the *r*-oriented samples, this thin film tilt – acting as an indicator for relaxation – increases with higher fluences. This is in contrast to the observation of decreasing relaxation with higher fluences due to increasing i.p. and o.o.p. strain. More investigations are needed to explain this effect.

In a qualitative sense, a similar behavior for *a*-plane samples is observed when investigating both in- and out-of-plane strain (Fig. 3.34b). However, the i.p. strain is 0.66 percentage points larger along the *y*-direction compared to *x*-direction for layers with less strain ($F = 0.7 \text{ J cm}^{-2}$). This discrepancy reduces for thin films that are more strained in total. Furthermore, as for the other orientations, the o.o.p. strain is systematically lower when compared to the values obtained from 2θ - ω -patterns, namely by 0.15 percentage points. The reasons for this effect are presumably the same as for the *m*-plane oriented samples. The shear and tilt angles for *a*-plane samples are depicted in Fig. 3.34b. As predicted by Grundmann [5], no tilt is observed along both the *x*-axis (< 1.5') and *y*-axis (< 0.7'). A small shear angle of around 1.5' is observed along the *y*-axis.

Finally, the mosaicity for both *m*- and *a*-plane samples is depicted in Fig. 3.29. For *m*-plane oriented samples, the ω -FWHM is approx. 40' and decreases slightly with higher fluences, which is in contrast to the increasing strain. For *a*-plane samples, a large spread similar to the samples of the 1st batch (cf. Fig. 3.27) is observed. But, again, this observation is probably due to the specific shape of ω -patterns for the *a*-plane samples. In Fig. B.5, the diffractograms are depicted and a severe deviation from the VOIGT shape can be identified. Therefore, determination of the FWHM is hindered and the large spread of values explained.

For two selected samples, Atomic Force Microscopy (AFM) measurements were performed by M. Sc. C. Dethloff and the height profiles are displayed as false color images in Fig. 3.35. The sample L.02 (Fig. 3.35a,b) was fabricated with a larger laser spot size compared to the sample L.05 (Fig. 3.35c,d). The Root Mean Square (RMS) roughness for each sample was determined from the topography of a $2 \times 2 \mu\text{m}^2$ and

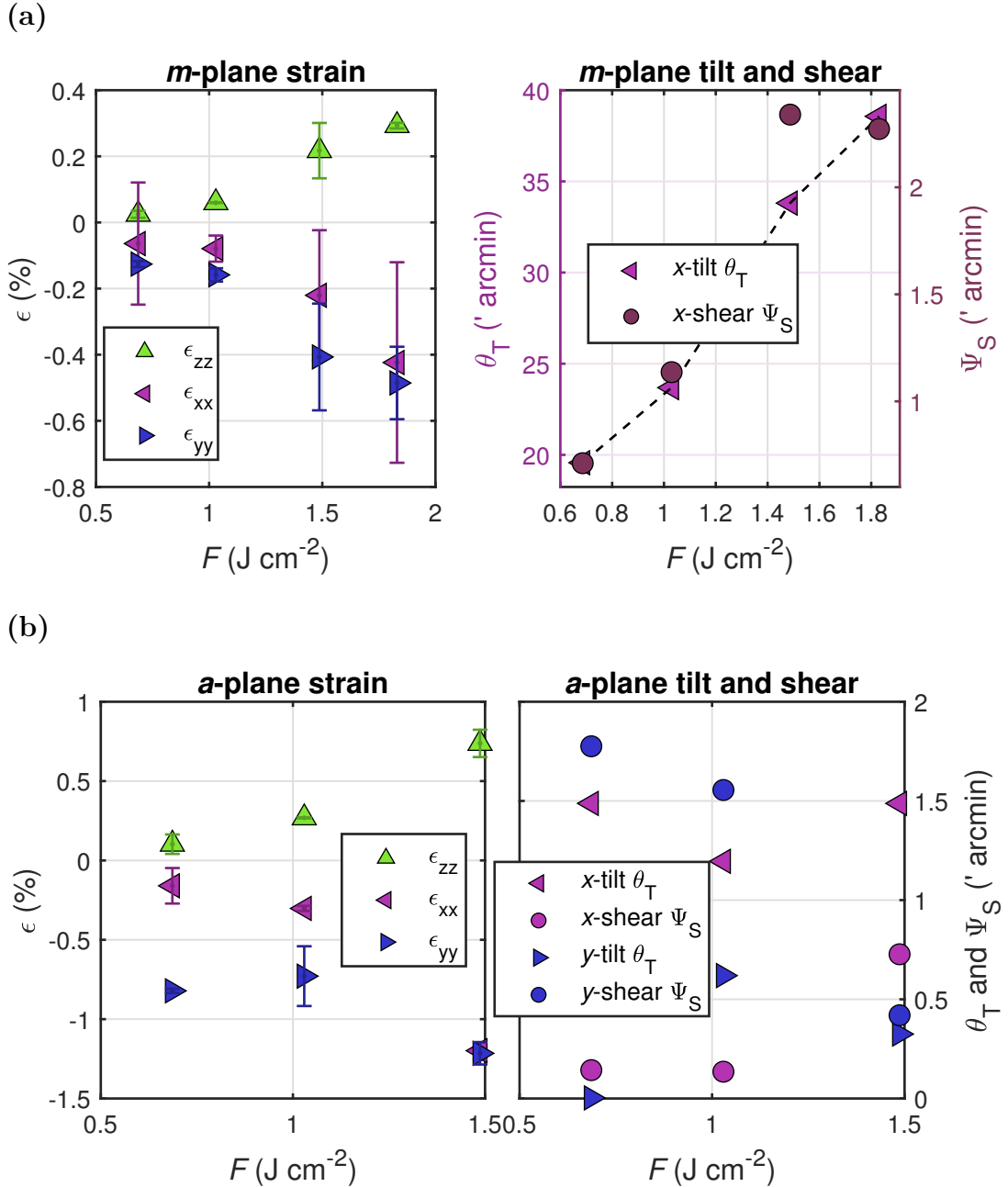


Figure 3.34: Left: In-plane (along x - and y -axis) and out-of-plane strain for the (a) m -oriented and (b) a -oriented samples from the 2nd batch, i.e. samples fabricated with varying laser pulse energy. The data was calculated from the peak positions of the RSMs described in section 3.3.1. Right: Shear (circles) and tilt (triangles) of thin films determined by asymmetric and symmetric reflections, respectively. The values were determined along x -axis and y -axis, but for m -plane samples, only the values along x -direction are shown.

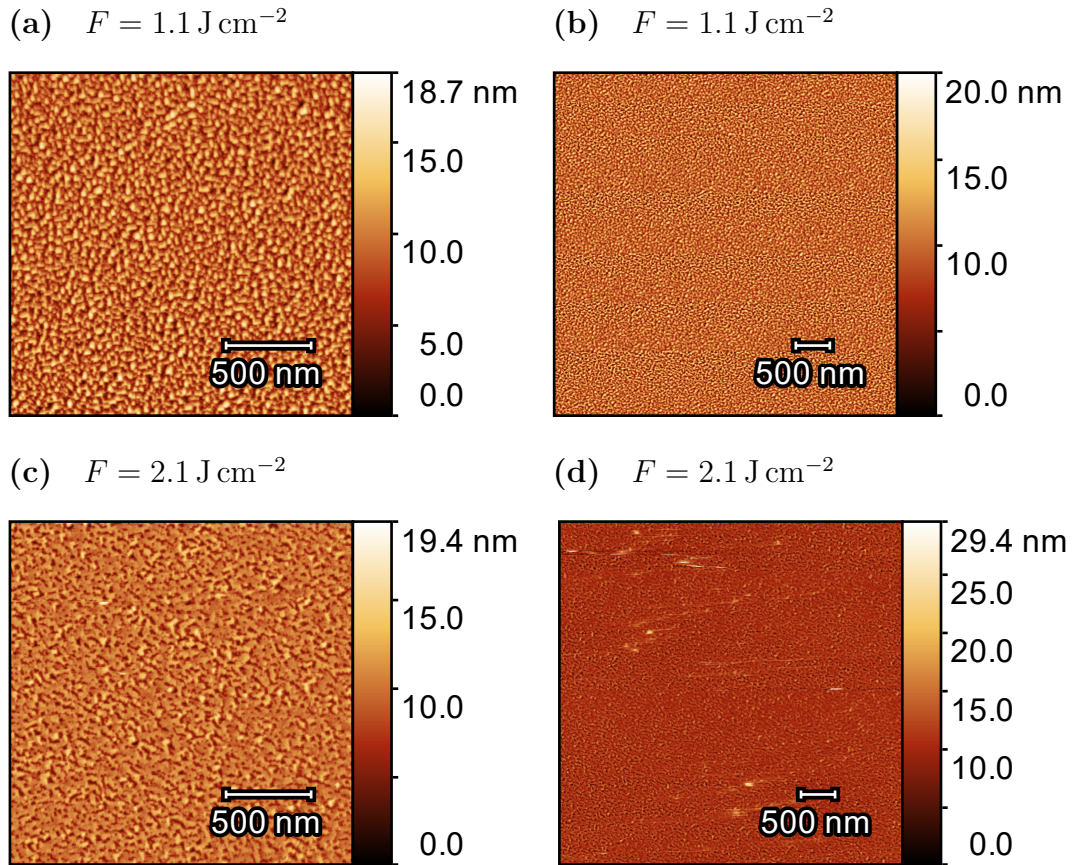


Figure 3.35: AFM false color images of two samples with (a, b) larger laser spot size and fluence of 1.1 J cm^{-2} (L.02) and (c, d) smaller laser spot size and laser fluence of 2.1 J cm^{-2} (L.05). The probed areas are $2 \times 2 \mu\text{m}^2$ and $5 \times 5 \mu\text{m}^2$ for the left and right panels, respectively.

Table 3.4: Strain, ω -FWHM and RMS roughness for two selected *m*-plane oriented Cr_2O_3 thin films that were investigated via AFM.

Id	thickness t	fluence F	strain ϵ_{zz}	ω -FWHM	RMS roughness
L.02	89 nm	1.05 J cm^{-2}	0.32 %	38.1'	2.5 nm
L.05	79 nm	2.06 J cm^{-2}	0.9 %	44.4'	1.9 nm

$5 \times 5 \mu\text{m}^2$ probed area. These values as well as other details are listed in Tab. 3.4. In general, the surface morphology is comparable to the results obtained before for α - Ga_2O_3 thin films fabricated by Pulsed Laser Deposition (PLD), where RMS roughnesses of 0.6 to 3.5 nm were achieved for different growth temperatures [7]. No significant difference in surface morphology could be observed for both samples. However, the sample fabricated with higher fluence L.05 exhibits several stripes on the surface (cf. Fig. 3.35d). They are presumably not a measurement artifact, because they remained during repeated scans of the surface (not shown). Therefore, although having slightly larger RMS roughness, the fabrication with larger laser spot size (L.02) yields more homogeneous surfaces.

In Fig. 3.36, the transmission spectra of selected *m*-plane oriented samples from the 1st batch are depicted. The fluence does not have a significant influence on the absorption onset, however, the thickness is decisive for the shape of the absorption edge, which is due to thin film interferences. The onset of absorption E_{opt} is approx.

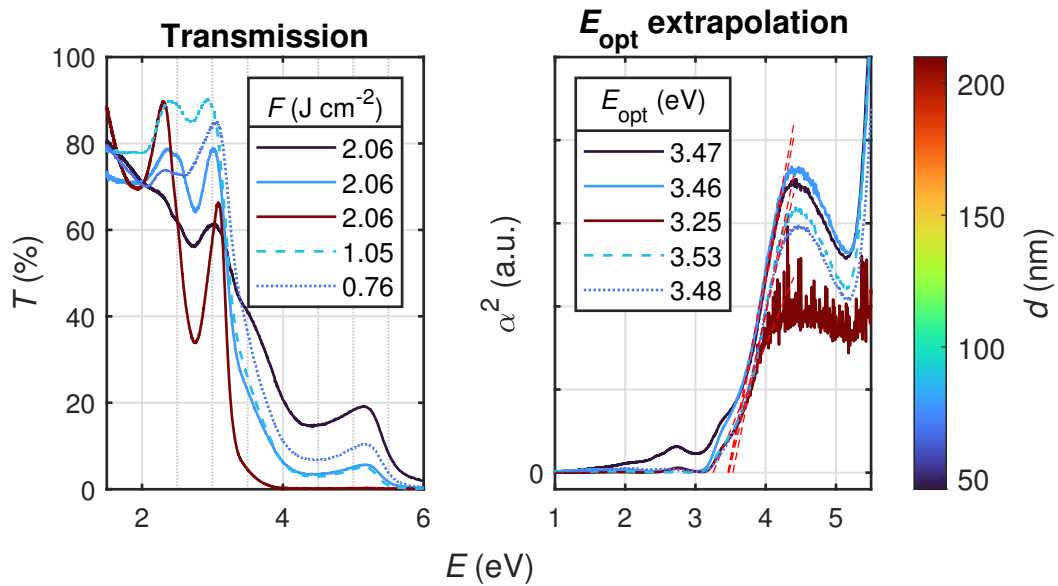


Figure 3.36: Transmission spectra (left) of selected m -plane oriented samples from the 1st batch. The samples differed in thickness and laser fluence on the target surface, achieved by varying lens positions. The α^2 vs. E plot (right) of the mentioned samples, determined by assuming a direct band gap of Cr_2O_3 (cf. 2.3.4 and 3.1).

3.5 eV for all samples of different thickness and fluence. This is in accordance with the value obtained for the samples of the initial Cr_2O_3 batch (cf. 3.1 and Fig. 3.6b).

3.3.4 Conclusion

The out-of-plane strain and in-plane strain of Cr_2O_3 thin films with different crystal orientations were investigated depending on the laser fluence on the target during deposition via PLD. The variation in laser fluence was achieved by either increasing the laser spot size or by decreasing the laser pulse energy. Samples with c -orientation grow fully pseudomorphic for low film thicknesses, whereas the samples with r -, m - and a -orientation are partially relaxed. The thickness is a crucial parameter for c - and r -plane samples, whereas the laser fluence on the target strongly influences the crystal structure of m - and a -plane samples. It can be concluded that the thickness of the thin films is more relevant for orientations that have more out-of-plane c -axis component. For c - and r -orientation, less laser fluence – no matter whether via larger laser spot sizes or reduced laser pulse energy – results in less FWHM in ω -patterns and thus better crystallinity. For m -plane samples, a reversed behavior is observed – however, the dependence on fluence is much less pronounced. A layered structure of a -plane thin films hardens the comparison of the ω -FWHM for this orientation. Furthermore, for r -, m - and a -plane oriented samples, thin film tilts have been observed in the directions that were previously observed for relaxed $\alpha\text{-Ga}_2\text{O}_3$ layers on Al_2O_3 [1, 6] (cf. Tab. 1.4b).

To understand the dependence between relaxation, crystallinity and thin film tilt for Cr_2O_3 m -plane thin films, a comparison to similarly structured $\alpha\text{-Ga}_2\text{O}_3$ can be made: In Kneiß *et al.* [6], fully relaxed m -plane $\alpha\text{-}(\text{Al}_x\text{Ga}_{1-x})_2\text{O}_3$ thin films exhibited a tilt that was dependent on the aluminum content, and therefore on relaxed lattice constants. For pure $\alpha\text{-Ga}_2\text{O}_3$ layers (zero aluminum content), a thin film tilt of 36' was observed, which is in accordance to the here observed angles of 20' to 40' (cf. Fig. 3.34a). In this work, however, due to variations in laser fluence, partially relaxed

m-plane Cr₂O₃ thin films with out-of-plane strain ranging from 0.02 % to 0.3 %⁽⁶⁾ could be fabricated (Fig. 3.34a). It was observed that samples with less out-of-plane strain – i.e. smaller out-of-plane lattice constants – exhibit smaller thin film tilts. Note that due to the fact that Al₂O₃ has smaller lattice constants than relaxed Cr₂O₃, a decrease in lattice constants is directly related to a decreasing mismatch between substrate and thin film. Therefore, the here reported results are in accordance to Kneiß *et al.* [6] in the sense that a reduction in lattice mismatch reduces the thin film tilt. Furthermore, reducing the laser fluence also results in a slightly higher ω -FWHM (Fig. 3.29), which could correspond to an increased dislocation density. When applying a heteroepitaxial model as displayed in Fig. 1.4 [8], this reduced dislocation density results in less thin film tilt, which is indeed observed. Therefore, an increasing laser fluence on the PLD target results in both increasing strain and decreasing ω -FWHM which manifest in larger thin film tilts. These effects can be summarized as less partially relaxed layers.

However, note that the importance of reduced laser fluence for more relaxed thin films is not explained yet. By taking the reduced kinetic energy of the plasma species into account [9], one can infer that the growth dynamics are altered in such a way that the formation of dislocations is favored. In general, note that more sophisticated methods like TEM should be applied to get a more detailed view into the formation and density of dislocations, which are fundamental to relaxation and thin film tilt.

No investigations of the influence of laser fluence on the structural properties of Cr₂O₃ thin films fabricated by PLD have been done so far in the literature. The only report on varying laser fluence from 1.6 to 3.7 J cm⁻² has been concerning the atomic ratio of Cr cations to O anions for deposition on silicon [10]. Most of the Cr₂O₃ thin films fabricated via PLD were deposited on *c*-plane sapphire [4, 11, 12]. None of those studies could identify the laser fluence as a crucial parameter influencing the crystallinity of the thin films (Fig. 3.29): the best ω -FWHM of 22' that was reported by Singh *et al.* [11] is larger than the here reported value of 7'. For *r*-plane oriented thin films reported by Punugupati *et al.* [13], an out-of-plane strain of 0.57 % could be identified, but no studies have been performed on the origin of this observation.

To determine the optimal deposition parameters of Cr₂O₃, one has to take the different orientations into account: Because the thickness is mostly relevant for *c*-plane oriented thin films, the choice of at least $t = 150$ nm results in the lowest strain and ω -FWHM. Furthermore, a laser spot size of 10 mm² and pulse energy of 300 mJ would result in the lowest strain for *r*-, *m*- and *a*-orientation. Note that this, however, results in less crystalline films for those orientations (Fig. 3.29), as well as a very low growth rate. Therefore, a pulse energy of 450 mJ is chosen for future depositions due to the best crystal quality while maintaining strain of about 0.1 % and 0.3 % for *m*- and *a*-plane respectively. Those deposition parameters also result in low thin film tilts of about 15' and 25' for *r*- and *m*-plane samples, respectively. The laser fluence on the target is therefore 1.1 J cm⁻², and will be applied when depositing high quality buffer layers for α -Ga₂O₃ thin films: The reduced compressive in-plane strain is desired to achieve low mismatch between the Cr₂O₃ and α -Ga₂O₃ layer, as demonstrated in the following chapter.

⁽⁶⁾ According the RSMs. Note that there was a discrepancy between the strain values obtained from 2θ - ω scans and RSMs.

Bibliography

- [1] M. Grundmann and M. Lorenz. “Anisotropic strain relaxation through prismatic and basal slip in α -(Al, Ga)₂O₃ on R-plane Al₂O₃”. In: *APL Materials* 8.2 (2020), p. 021108. ISSN: 2166-532X. DOI: [10.1063/1.5144744](https://doi.org/10.1063/1.5144744).
- [2] M W Cho *et al.* “ZnO epitaxial layers grown on c-sapphire substrate with MgO buffer by plasma-assisted molecular beam epitaxy (P-MBE)”. In: *Semiconductor Science and Technology* 20.4 (2005), S13–S21. ISSN: 0268-1242, 1361-6641. DOI: [10.1088/0268-1242/20/4/002](https://doi.org/10.1088/0268-1242/20/4/002).
- [3] O. Durand *et al.* “Interpretation of the two-components observed in high resolution X-ray diffraction ω scan peaks for mosaic ZnO thin films grown on c-sapphire substrates using pulsed laser deposition”. In: *Thin Solid Films* 519.19 (2011), pp. 6369–6373. ISSN: 00406090. DOI: [10.1016/j.tsf.2011.04.036](https://doi.org/10.1016/j.tsf.2011.04.036).
- [4] Elisabetta Arca *et al.* “Valence band modification of Cr₂O₃ by Ni-doping: creating a high figure of merit *p*-type TCO”. In: *Journal of Materials Chemistry C* 5.47 (2017), pp. 12610–12618. ISSN: 2050-7534. DOI: [10.1039/C7TC03545D](https://doi.org/10.1039/C7TC03545D).
- [5] Marius Grundmann. “Elastic theory of pseudomorphic monoclinic and rhombohedral heterostructures”. In: *Journal of Applied Physics* 124.18 (2018), p. 185302. ISSN: 0021-8979, 1089-7550. DOI: [10.1063/1.5045845](https://doi.org/10.1063/1.5045845).
- [6] Max Kneiß *et al.* “Strain states and relaxation for α -(Al_xGa_{1-x})₂O₃ thin films on prismatic planes of α -Al₂O₃ in the full composition range: Fundamental difference of a- and m-epitaxial planes in the manifestation of shear strain and lattice tilt”. In: *Journal of Materials Research* 36.23 (2021), pp. 4816–4831. ISSN: 0884-2914, 2044-5326. DOI: [10.1557/s43578-021-00375-3](https://doi.org/10.1557/s43578-021-00375-3).
- [7] Clemens Petersen *et al.* “PLD of α -Ga₂O₃ on m-plane Al₂O₃: Growth regime, growth process, and structural properties”. In: *APL Materials* 11.6 (2023), p. 061122. ISSN: 2166-532X. DOI: [10.1063/5.0149797](https://doi.org/10.1063/5.0149797).
- [8] Marius Grundmann. *The Physics of Semiconductors: An Introduction Including Nanophysics and Applications*. Graduate Texts in Physics. Cham: Springer International Publishing, 2016. ISBN: 978-3-319-23879-1 978-3-319-23880-7. URL: <http://link.springer.com/10.1007/978-3-319-23880-7>.
- [9] S.I. Anisimov, B.S. Luk'yanchuk, and A. Luches. “An analytical model for three-dimensional laser plume expansion into vacuum in hydrodynamic regime”. In: *Applied Surface Science* 96–98 (1996), pp. 24–32. ISSN: 01694332. DOI: [10.1016/0169-4332\(95\)00373-8](https://doi.org/10.1016/0169-4332(95)00373-8).
- [10] M. Tabbal *et al.* “Pulsed laser deposition of nanostructured dichromium trioxide thin films”. In: *Thin Solid Films* 515.4 (2006), pp. 1976–1984. ISSN: 00406090. DOI: [10.1016/j.tsf.2006.08.010](https://doi.org/10.1016/j.tsf.2006.08.010).

- [11] Jarnail Singh *et al.* “Structural, optical and electrical characterization of epitaxial Cr₂O₃ thin film deposited by PLD”. In: *Materials Research Express* 6.10 (2019), p. 106406. ISSN: 2053-1591. DOI: [10.1088/2053-1591/ab3543](https://doi.org/10.1088/2053-1591/ab3543).
- [12] Aoife B Kehoe *et al.* “Assessing the potential of Mg-doped Cr₂O₃ as a novel *p*-type transparent conducting oxide”. In: *Journal of Physics: Condensed Matter* 28.12 (2016), p. 125501. ISSN: 0953-8984, 1361-648X. DOI: [10.1088/0953-8984/28/12/125501](https://doi.org/10.1088/0953-8984/28/12/125501).
- [13] Sandhyarani Punugupati, Jagdish Narayan, and Frank Hunte. “Room temperature ferromagnetism in epitaxial Cr₂O₃ thin films grown on r-sapphire”. In: *Journal of Applied Physics* 117.19 (2015), p. 193907. ISSN: 0021-8979, 1089-7550. DOI: [10.1063/1.4921435](https://doi.org/10.1063/1.4921435).